

Journal of Geophysical Research: Atmospheres

RESEARCH ARTICLE

10.1029/2017JD027503

Key Points:

- Cyclones do not always respond to the SST anomaly in the Sea of Japan
- A cooled Sea of Japan provides both strengthening and weakening effects
- Modulations depend on atmospheric background and dynamics of the cyclone development

Supporting Information:

- Supporting Information S1

Correspondence to:

N. Zhao,
ningz1120@riam.kyushu-u.ac.jp

Citation:

Zhao, N., Iwasaki, S., Yamamoto, M., & Isobe, A. (2018). Modulation of extratropical cyclones by previous cyclones via the sea surface temperature anomaly over the Sea of Japan in winter. *Journal of Geophysical Research: Atmospheres*, 123. <https://doi.org/10.1029/2017JD027503>

Received 24 JUL 2017

Accepted 13 MAY 2018

Accepted article online 18 MAY 2018

Modulation of Extratropical Cyclones by Previous Cyclones via the Sea Surface Temperature Anomaly Over the Sea of Japan in Winter

Ning Zhao^{1,2} , Shinsuke Iwasaki³, Masaru Yamamoto² , and Atsuhiro Isobe² 

¹Interdisciplinary Graduate School of Engineering Sciences, Kyushu University, Kasuga, Japan, ²Research Institute for Applied Mechanics, Kyushu University, Kasuga, Japan, ³Civil Engineering Research Institute for Cold Region, Sapporo, Japan

Abstract The effects of a cyclone-induced sea surface temperature (SST) anomaly in the Sea of Japan on following cyclones were investigated using a regional numerical model. The model was conducted with and without an SST anomaly due to cooling from a single extratropical cyclone in winter. Twenty-six pairs of sensitivity experiments demonstrated that cyclones were not always sensitive to the SST anomaly. The low-level trough (strong northwesterly winds) affected cyclone sensitivity via a cold air intrusion over the Sea of Japan. A strong (weak) cold air intrusion formed a relatively unstable (stable) and higher (lower) convective layer and the concentration of cyclone paths over the oceans, making the cyclones sensitive to the underlying SST. Two specific cyclones were analyzed to demonstrate two distinct patterns (wave-like and path shifting, respectively) in cyclone modulations revealed in the wavelet spectra. The wave-like pattern was formed by the superposition of multiple anomalous waves with different periods and scales, which originated from upper-level potential vorticity anomalies and temperature advection. The path-shifting pattern was caused by the diabatic heating-induced potential vorticity anomalies, which were supplied by the intense heat and moisture from the regions surrounding the Sea of Japan. Therefore, a cyclone can modulate a following cyclone by reducing the SST over the Sea of Japan; however, the modulation can vary in different ways, depending on the atmospheric background and dynamics of the cyclone development.

1. Introduction

Extratropical cyclones have been recognized as a vital component of both midlatitude weather systems and global circulation (e.g., Catto et al., 2012; Chang et al., 2002). These synoptic phenomena transport large amounts of moisture and energy while strongly interacting with the sea underneath. Because of the strong air-sea heat and moisture exchange along the Kuroshio and its extension, namely, the anchoring effect (e.g., Nakamura et al., 2004), East Asia is one of the most active areas for extratropical cyclones based on statistical and numerical studies, especially in winter (Pinto et al., 2007; Roebber, 1984; Shaw et al., 2016).

It is well known that sea surface temperature (SST) features, such as, oceanic fronts (i.e., the SST gradient), are critical for cyclone development (e.g., Kwon et al., 2010; Small et al., 2008, and references therein). Sensitivity studies have demonstrated that a strong (weak) SST gradient can lead to intensified (weakened) cyclone activity and a poleward (equatorward) shift of storm tracks (Brayshaw et al., 2008; Sampe et al., 2010). Moreover, based on both observed and modeled evidence, some recent studies have demonstrated that mesoscale SST features have a large impact on air-sea interactions (e.g., Chelton & Xie, 2010; Putrasahan et al., 2013; Masunaga et al., 2016) and therefore cyclogenesis (e.g., Ma et al., 2017; Willison et al., 2013).

In addition to the Kuroshio, the SST over the East Asian marginal seas may play a significant role in cyclone activities in the western North Pacific, as well as cyclone activity above the marginal seas. This is because these seas are located in a transition zone linking the cool and dry Asian continent and the warm and moist North Pacific, especially in winter. These marginal seas are therefore important for the local atmosphere, including the lower-level baroclinity and cyclogenesis (e.g., Chen et al., 2001; Isobe & Kako, 2012; Yamamoto & Hirose, 2007, 2011). Furthermore, upstream of the storm tracks in the western North Pacific, changes in sea properties (e.g., SST) can spread to a much larger area via the interactions with eastward-propagating cyclones (e.g., Hirose et al., 2009; Kelly et al., 2010; Seo et al., 2014).

Because of the relatively weak ocean currents (and therefore, small heat transport) in the marginal seas, these areas are more sensitive to the cyclone-induced surface heat flux than the Kuroshio region. Among such seas, the Sea of Japan, which is the focus of this study, may be the most active region of air-sea interactions in East Asia, especially during winter when the strong monsoon conveys the cold air mass into the whole of East Asia (e.g., Nakamura, 1992; Nakamura et al., 2002). Zhao et al. (2016) showed that the Sea of Japan experienced strong surface cooling due to a single cyclone that reduced the SST by less than -0.5°C around the subpolar front ($\sim 0.25^{\circ}\text{C}$ averaged over the Sea of Japan) and that this SST reduction was sustained over the course of 4 days.

These atmospheric and oceanic responses in both directions suggest that the Sea of Japan becomes a link between two consecutive cyclones. That is, an extratropical cyclone passing over the Sea of Japan modulates the following cyclone passing along the same track via the SST reduction. This likely occurs because the length of the SST reduction (>4 days) is comparable with the sub-weekly scale of the interval of extratropical cyclones. Yet it is still unknown whether this small (-0.25°C on average) and basin-scale temperature anomaly can cause any detectable modifications in the synoptic scale atmospheric circulation. If this is the case, it is worthwhile investigating how the Sea of Japan affects the following cyclone. Based on a regional numerical experiment as a case study, Yamamoto (2013) suggested that a colder Sea of Japan would weaken the baroclinic wave at the early stage of cyclogenesis and generate a “Western Pacific pattern-like” anomaly in the geopotential height. However, they mainly studied a dynamic process that occurs within the area around a cyclone, without focusing on larger-scale background factors, which may have influences on cyclogenesis, or even conditions before the cyclone was generated (e.g., Kuwano-Yoshida & Asuma, 2004; Yoshiike & Kawamura, 2009). Therefore, it is necessary to explore further whether the weakening effect mentioned by Yamamoto (2013) occurs commonly in cyclones from various backgrounds.

In the present study, we focused on two scientific questions: (1) Does the cyclone-induced SST anomaly in the Sea of Japan affect all passing cyclones? (2) Does cooling in the Sea of Japan weaken all passing cyclones, as Yamamoto (2013) suggested? Following the approach taken by Yamamoto (2013), we conducted numerical experiments on individual cyclones using a regional model to understand the possible role of the Sea of Japan in wintertime extratropical cyclones.

This paper is organized as follows. Section 2 explains the data sources, the model setup, and the algorithms used for detecting and characterizing cyclones. Section 3 describes the modeled cyclone responses, which answers the first question mentioned above. Section 4 shows what effect a cooled Sea of Japan could have on cyclone activities related to the second question. In section 5, we analyzed two sample cyclones in detail, with the analysis suggesting that different cyclone dynamics originated from the cooled Sea of Japan. Finally, a summary of the major findings is presented in section 6.

2. Materials and Methods

2.1. Data Sources

We analyzed the 6-hourly National Centers for Environmental Prediction (NCEP) Final (FNL) Operational Global Analysis data (NCEP, 2000). The FNL data set has a horizontal resolution of 1° in latitude and longitude and 27 vertical layers from the surface to 10 hPa. The period considered was used from November 2003 to February 2011, as in the work of Zhao et al. (2016). In addition to the preprocessing of cyclone detection (see the next subsection), this data set was used to set initial and lateral boundary conditions in the numerical model. The Optimum Interpolation SST (OISST) was used for the lower boundary conditions, and its horizontal resolution is 0.25° in both latitude and longitude (Banzon et al., 2016; Reynolds et al., 2007).

2.2. Tracking Centers and Paths

For consistency with the numerical sensitivity experiments on the SST modification described in the next subsection, we used the sea-level pressure (SLP) from NCEP-FNL to track extratropical cyclones near the Sea of Japan ($115^{\circ} - 170^{\circ}\text{E}, 25^{\circ} - 60^{\circ}\text{N}$) during the eight winters from November to February, 2003–2011. We adopted one of the most straightforward methods for identifying and tracking the cyclones among the various methods established to date (e.g., Flaounas et al., 2014; Hodges, 1999; Inatsu, 2009). First, the cyclone centers were identified as the local minima where the SLP was reduced by 0.5 hPa compared with that in the neighboring eight grids (i.e., within a $3^{\circ} \times 3^{\circ}$ box in the FNL data set), and all centers less than 1,010 hPa were recorded. Thereafter, we searched for the center of the same cyclone after 6 hr on a $10^{\circ} \times 7^{\circ}$ longitude-latitude box, that is, slightly larger than that in the work of Flaounas et al. (2014), where the center was identical to the

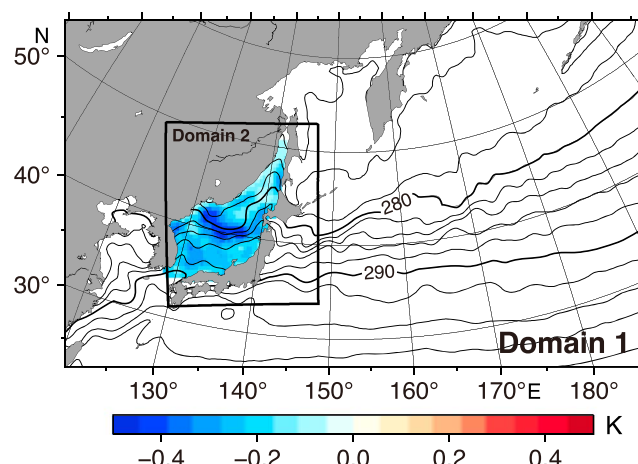


Figure 1. WRF model domains overlapped by the climatological mean SST during the winters (NDJF) of 2003–2011. Colored shading shows the SST anomaly used in the LSST runs. SST = sea surface temperature; WRF = weather research and forecast.

cyclone center in the previous time step. The tracking of cyclone centers was continued until the cyclone moved beyond the lateral boundary of Domain 1 in Figure 1, or vanished. All cyclones with a lifetime of less than 24 hr were removed. Finally, among the 136 cyclones that were identified, we randomly chose 26 for the sensitivity experiments. The randomly selected cyclones were therefore not concentrated around specific trajectories or times. The temporal coverage of selected cyclones is listed in Table 1, and the spatial coverage is shown later in Figure 2. When tracking the simulated cyclones, the SLP criterion for cyclone center tracking was changed from 0.5 hPa to the local minimum due to the much higher resolution of the numerical model than the NCEP-FNL data set.

2.3. Model Setup of the Sensitivity Experiment

Following Yamamoto (2013), the numerical sensitivity experiments, including a large domain covering the western Pacific Ocean and a two-way nested domain covering the Sea of Japan, were conducted using the weather research and forecast (WRF) model version 3.7.1 (Skamarock et al., 2008). The model domains are shown in Figure 1, and the resolutions are listed in Table 2.

Two sets of numerical experiments were conducted to answer the two questions as mentioned in the Introduction. First, for comparison, controlled experiments to reproduce the 26 selected cyclones were conducted (hereinafter, “CNTL” runs), where the climatological winter SST averaged from 2003 to 2011 was set as the lower boundary (contours in Figure 1) for simplicity. Second, the same experiments were conducted, except that a negative SST anomaly (colored shading in Figure 1) was set for the Sea of Japan (i.e., a low SST run, hereinafter, “LSST” runs). This anomaly was obtained from Zhao et al. (2016), who computed the SST reduction caused by the passage of a single cyclone over the Sea of Japan. We therefore referred to this modeling

Table 1
Temporal Coverage of 26 Selected Cyclones

Year	Number	Month	Number
2003	2	Nov	5
2004	5	Dec	4
2005	1	Jan	8
2006	3	Feb	9
2007	1	Total	26
2008	4		
2009	3		
2010	2		
2011	5		
Total	26		

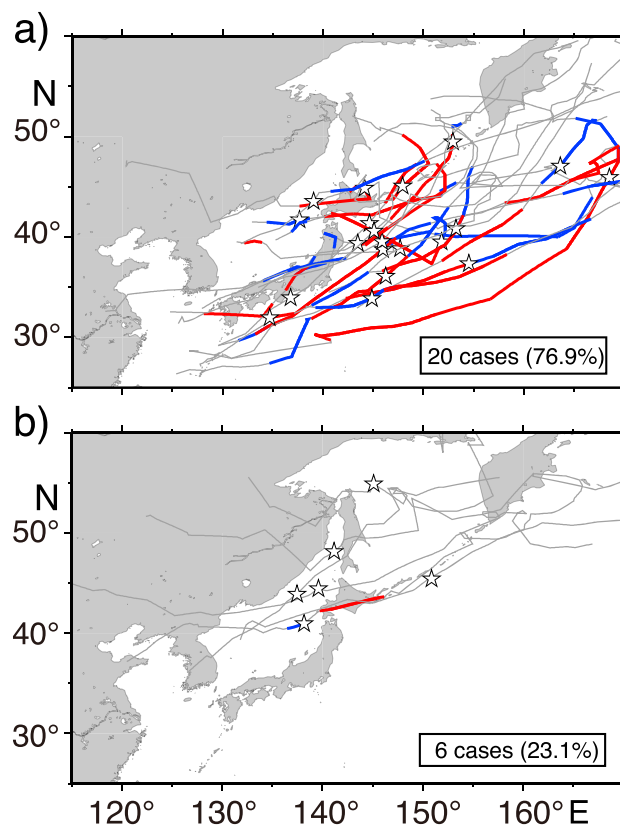


Figure 2. Paths of the simulated cyclones in the CNTL runs: (a) 20 affected cyclones and (b) six unaffected cyclones. Red curves show the strengthening periods (>0.1 Bergeron), and blue curves show the weakening periods (less than -0.1 Bergeron). Stars indicate the locations of the maximum CDR for each cyclone. See text for details on the CDR. CDR = cyclone deepening rate.

as the sensitivity experiment, because the modeled difference between the CNTL and LSST runs showed the influence of a cyclone that had passed previously on the following cyclone via SST in the Sea of Japan. All calculations began 4 days before the target cyclone was formed (or appeared out of a cyclone center detected by the algorithm described above), and the modeling thereafter continued during the subsequent 9 days. The modeled atmospheric properties were saved every 3 hr over the course of each computation.

The objective of the study was to evaluate cyclone responses to the cyclone-induced SST anomaly. Therefore, the SST field set for the CNTL runs was common among all of the combinations of LSST and CNTL runs; otherwise, the responses could not be distinguished from those derived from the intraseasonal and/or interannual SST variation. Therefore, it was difficult to validate our results using the observations and/or reanalysis data associated with the actual SST field. Nevertheless, our results were likely to be reliable because the ensemble simulations produced a robust result (see Appendix A for details).

2.4. Indicators of the Effect on Cyclones

In general, the development of an extratropical cyclone can be evaluated by the deepening rate of the central SLP. In this study, the 12-hr cyclone deepening rate (CDR; Kuwano-Yoshida & Asuma, 2004) was calculated for all cyclones, and the changes of CDRs in the two runs were used to show to what extent the cyclones were modified. The CDR formula in Bergeron (hPa/hr) can be written as follows:

$$CDR = \left[\frac{p(t-6) - p(t+6)}{12} \right] \frac{\sin 60^\circ}{\frac{\sin \phi(t-6) - \phi(t+6)}{2}}, \quad (1)$$

where p is the SLP at the cyclone center, ϕ is the latitude, and t is the time. We introduced three criteria to estimate the modifications based on their differences ($\Delta CDR = CDR_{LSST} - CDR_{CNTL}$), where the subscripts denote the LSST and CNTL runs, respectively. The cyclones were categorized as "affected" cyclones when they

Table 2
Settings of Two Runs Performed by WRFV3

Run	CNTL	LSST
Domain	Domain 1: 230 × 132 (30 km) Domain 2: 181 × 217 (10 km)	
Vertical resolution	35 sigma layers	
Period	9 days for each cyclone with prior 4 days for spinning up	
Lower boundary	Winter climatological SST (contour in Figure 1)	With extra Δ SST (shading in Figure 1)

met these three conditions: $|\Delta CDR| > 0.1$, $CDR_{\text{CNTL}} > 0.5$, and a duration longer than 6 hr, which enabled the removal of occasional events. The other cyclones were referred to as “unaffected.” The results were mostly independent of the lower limit of CDR_{CNTL} (e.g., set from 0.5 to 0), and $|\Delta CDR| > 0.1$ was chosen to remove the unexpected small disturbances.

It is possible that the deepening rate could only identify the local changes at the center of cyclones. Therefore, we also used the standard deviation (SD) of the geopotential height to validate the results based on CDRs (e.g., Chang et al., 2002; König et al., 1993). The SDs were calculated using the geopotential height at the 850-hPa level during the cyclone’s life span, and the unfiltered geopotential heights were used in the following analyses. Similar results were found when using the 1- to 8-day band-pass filtered geopotential height (not shown). Note that the same cyclone in the CNTL and LSST runs had the same life span.

Furthermore, to evaluate the detailed response of the affected cyclones, we performed a Morlet wavelet analysis (Torrence & Compo, 1998) on the time series of geopotential heights. The aim of this analysis was to show the activities of the baroclinic wave, especially during the early developmental stage of cyclones. Specifically, we chose a time series of geopotential heights above the surface cyclone centers at 6 hr after their maximum CDRs (i.e., sufficient development of the cyclone; see the definition of our 12-hr CDR).

3. Did All Cyclones Respond to the SST Anomaly?

3.1. Basic Results

Among the 26 simulated cyclones, 20 (76.9%) were significantly affected by the cold Sea of Japan, while the remaining six (23.1%) were almost unaffected. Figure 2 shows the paths of these cyclones. A similar separation of “affected” cyclones and “unaffected” cyclones was found based on the difference in the SD (LSST-CNTL runs) of the geopotential height at the 850-hPa level (see Figure S1 in the supporting information), suggesting that the results based on CDRs were reliable.

The affected cyclones (Figure 2a) were mostly located in the southern domain compared with those of the unaffected cyclones (Figure 2b), while the locations of their maximum CDRs were concentrated in the western North Pacific (stars in Figure 2a). These cyclones passed through the downstream of the winter monsoon, which may be the carrier of the influences from the Sea of Japan. In contrast, the unaffected cyclones developed mostly over the Sea of Japan or the Sea of Okhotsk (Figure 2b), passing through upstream of the winter monsoon, and were unlikely to be sensitive to the SST reduction of the relatively small Sea of Japan. As suggested in some previous studies (e.g., Yoshiike & Kawamura, 2009), differences in cyclone paths were also strongly related to the winter monsoon and other large-scale atmospheric features, such as the location of troughs or westerly winds. Therefore, we suggest a potential connection between the cyclone sensitivity to the SST anomaly and the atmospheric background. Note that we found no clear difference in the deepening rate and time coverage between the affected and unaffected cyclones. Additionally, it is possible that the unaffected cyclones were similar to the OJ-type cyclones, as defined by Kuwano-Yoshida and Asuma (2004), which were not so sensitive to the moisture amount and therefore the SST anomaly. However, this was not the case in this study, because we found that the OJ-type cyclone could also be clearly modified by the SST anomaly (e.g., the example cyclone shown later in section 5.1).

3.2. Switching of Cyclone Sensitivity

Figure 3a shows composite maps of the lower-level potential temperature anomalies (LSST-CNTL runs) of the affected and unaffected cyclones during the 4 days prior to cyclone generation, along with the geopotential

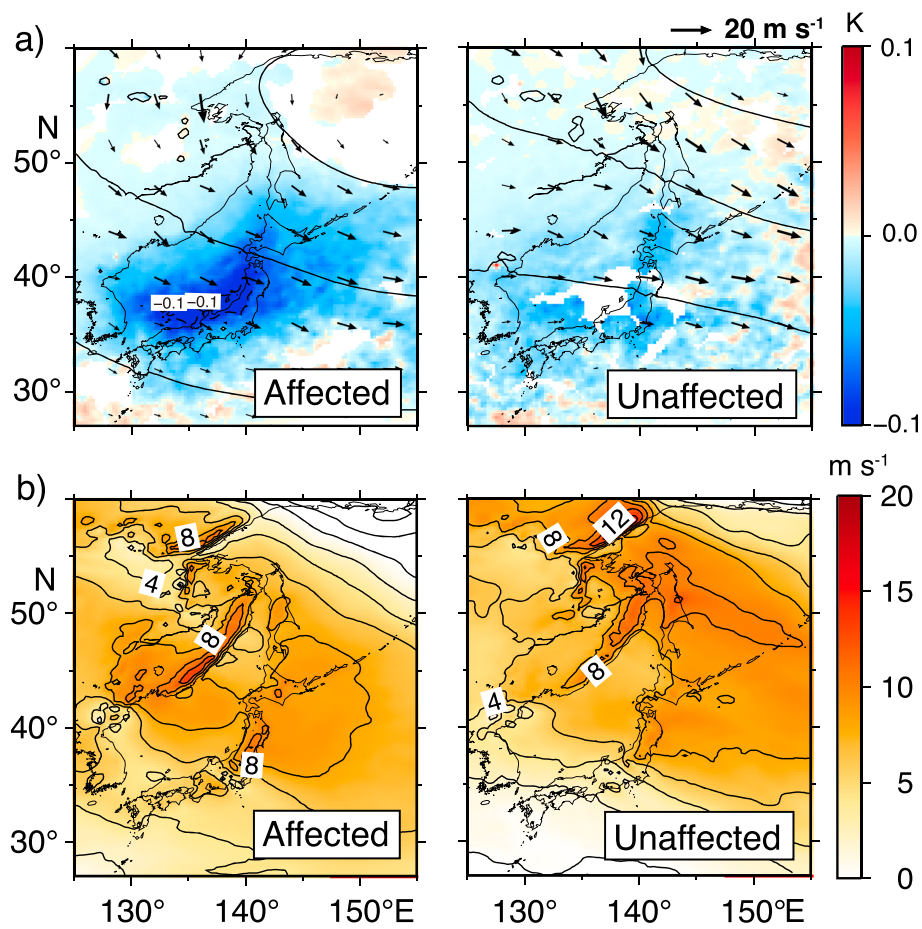


Figure 3. Composite maps of the potential temperature anomalies (LSST–CNTL runs) and winds in the CNTL runs, which were averaged during the 4 days prior to the cyclone generation. Maps for the affected (unaffected) cyclones are shown in the left (right) panel. Panel (a) indicates the potential temperature anomalies at the 850-hPa level (colored shading and dashed contours; only significant values are plotted), along with the geopotential height (thin solid contours) and wind vectors in the CNTL runs. Panel (b) denotes the horizontal distribution of the southeastward component of the 10-m wind. The contour intervals are 0.1 K and 100 m in panel (a), and 2 m/s in panel (b).

height and wind vectors in the CNTL runs. Considering that the SST anomaly applied in the LSST runs was approximately -0.25°C on average, we found that the local atmosphere was cooled over 0.1 K by the SST anomaly before the affected cyclones were generated (90% confidence level or greater based on a Student's *t* test). Conversely, the temperature reduction was fairly small in the case of unaffected cyclones (weak and insignificant).

Before the affected (unaffected) cyclones were generated, a deeper (shallower) lower-level trough over the Sea of Japan induced a strong wind that moved over the Sea of Japan (the Sea of Okhotsk); see the contours of geopotential heights (Figure 3a) and the magnitude of the southeastward component of the 10-m wind (Figure 3b) in the CNTL runs. These differences in the lower-level atmosphere did not change even if the composite maps were produced for the entire simulation period (not shown), suggesting that they were controlled by a large-scale phenomenon rather than the cyclone itself. Note that these structures of low-level troughs and the wind field were not changed in LSST runs.

The strong northwesterly winds, before the cyclone was generated, conveyed a colder air mass onto the Sea of Japan. Figure 4a shows the composite maps of equivalent potential temperature (θ_e) and its horizontal gradient, $|\nabla\theta_e|$, at the 850-hPa level with the same duration as in Figure 3. Comparing with the unaffected cyclones, the Sea of Japan in the affected-cyclone cases was covered by an atmosphere colder by over 8 K (right panels in Figure 4).

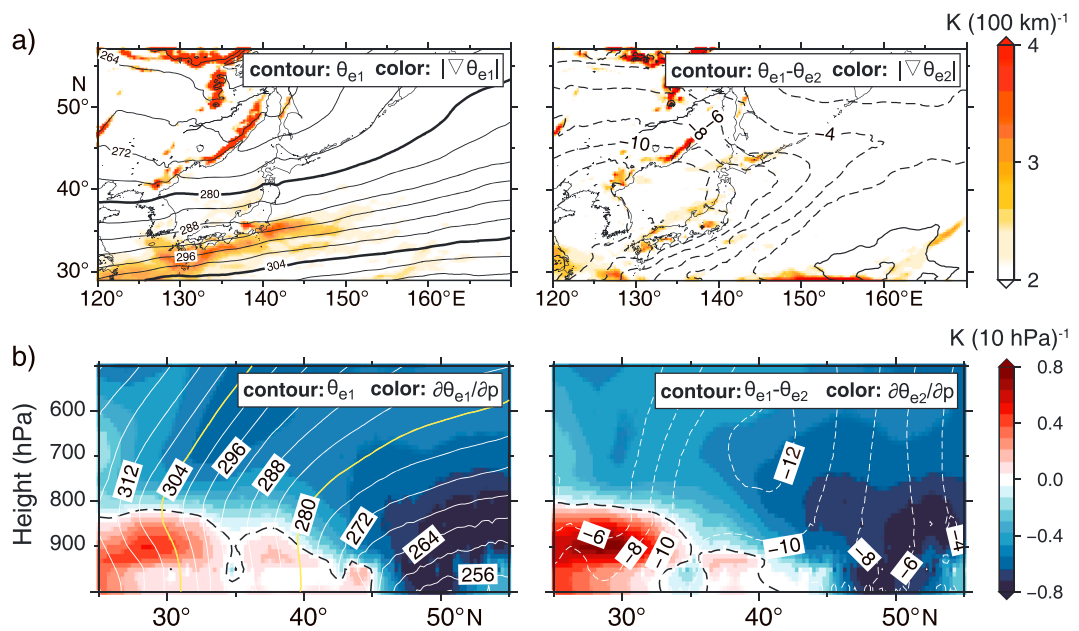


Figure 4. Composite maps of low-level horizontal (a) and vertical (b; averaged over 130°–140°E) thermal structure of the atmosphere above the Sea of Japan in the CNTL runs and the differences between two runs (LSST-CNTL runs). θ_{e1} and θ_{e2} represent the equivalent potential temperature in affected and unaffected cases, respectively. Contours show θ_{e1} (left panels) and the difference between θ_{e1} and θ_{e2} (right panels). Colored shading shows the gradients of θ_{e1} (left panels) and θ_{e2} (right panels). Contour intervals are 4 K in the left panels and 2 K in the right panels.

This southeastward migration of the cold air-mass intensified the lower-level baroclinity south of Japan just above the warm Kuroshio current, while the baroclinity was mostly undetectable in the unaffected cases (colored shading in Figure 4a). Such conditions are favorable for air-sea interactions around oceanic fronts (Parfitt et al., 2016) and for cyclogenesis, leading to the occurrence of storm tracks (Figure 2a). Similar structures were visible even after the cyclone passed (not shown), suggesting that these conditions were related to the low frequency variability in the atmosphere, not to a single cyclone. As a result, the cyclones concentrated in the south, making them sensitive to the changes in moisture and surface heat supplemented from the underlying ocean.

Furthermore, owing to this cold air mass, the Sea of Japan heated and destabilized the atmosphere aloft in the affected cyclone cases more intensively, inducing strong convection and vertical mixing within the marine atmospheric boundary layer. Figure 4b shows the vertical thermal structures of the atmosphere over the Sea of Japan. In general, warm oceans make the marine atmospheric boundary layer unstable because of enhanced winter convection. Therefore, it is likely that the enhanced winter convection in the affected cyclone cases effectively mixed the lower-layer atmosphere, and thus, the marine atmospheric boundary layer reached a higher level than an unaffected case. For example, see the higher heights of the dashed curves (zero contours of stability) in the affected case compared with the unaffected case over the Sea of Japan (35°–45°N; Figure 4b). The affected cyclones could therefore be more sensitive to the lower boundary conditions (i.e., the SST in this study) via these processes.

4. Nonmonotonic Effects of the Cooled Sea of Japan

Based on the criteria defined in section 2.4, the life span of each affected cyclone can be further categorized into a strengthening period ($\Delta CDR > 0.1$) and a weakening period ($\Delta CDR < -0.1$). As shown in Figure 2a, the red and blue lines that represent the two different periods are interleaved with each other, suggesting that the influences of the cooled Sea of Japan are much more complex than a simple monotonic strengthening or weakening. Note that the paths with no red or blue colors in Figure 2 show the periods when the cyclone was not obviously changed ($|\Delta CDR| < 0.1$).

Further evidence could be found from the results of wavelet analyses. Figures 5 and 6 show the anomalies (LSST-CNTL runs) of the wavelet spectra of all 20 affected cyclones at the 850- and 500-hPa levels, respectively.

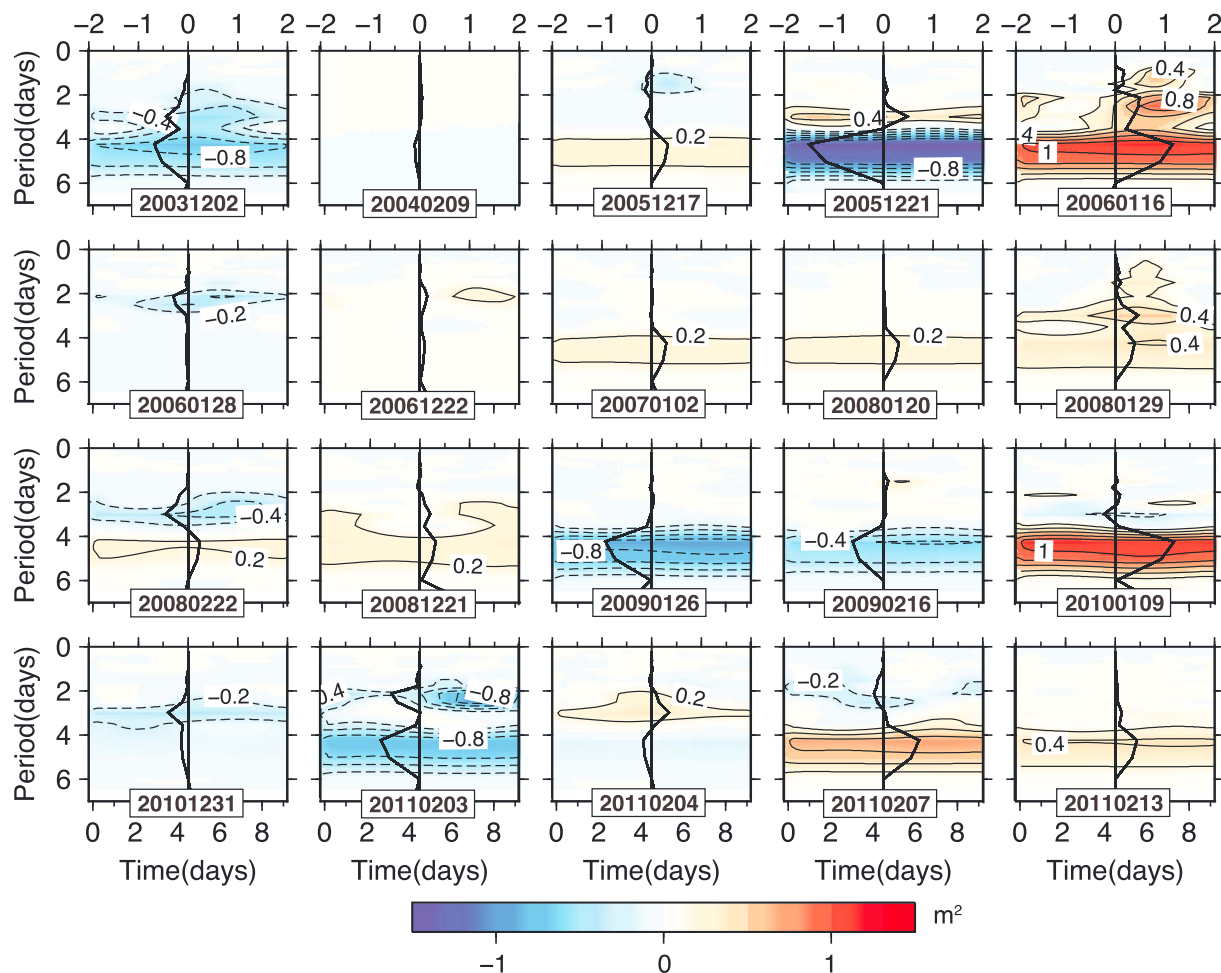


Figure 5. Differences (LSST-CNTL runs) in the normalized wavelet power spectra of geopotential heights at the 850-hPa level for 20 affected cyclones. The thick solid curves, together with the upper axes, show the global means of the differences in each panel. The year/month/date at the beginning of the computations are shown in each panel. Contour intervals are 0.2 m^2 for values $< \pm 1 \text{ m}^2$, and 0.5 m^2 for $> \pm 1 \text{ m}^2$.

Although there were a variety of patterns in the wavelet spectra, most of the changes were concentrated around 4.5 days, and both intensified and weakened signals were observed (see the peaks of the global means). The wavelet spectra at both the 850-hPa and the 500-hPa levels in the CNTL runs showed that the baroclinic waves had a major wave period at 4.5 days but with a wider distribution ranging from 2 to 6 days (the typical time scale for synoptic eddies, not shown). Therefore, the anomalies of the wavelet spectra suggested that a cooled Sea of Japan could act as both a strengthening and a weakening factor on passing cyclones.

In addition to the modulations of cyclones (~ 4.5 days), the anomalous energy in the short-duration motions ($2\sim 3$ days) at both the 850-hPa and the 500-hPa levels was also strong. The simultaneous appearance of both the positive and negative anomalies on each panel of the wavelet spectra suggests that the cooled Sea of Japan could generate or modulate waves in different frequencies (e.g., panels for 20051221 in Figures 5 and 6). Likewise, the inconsistency of the anomalies at different levels in the same period also suggested that these anomalous waves may propagate in different directions (upward or downward) and/or be generated by different mechanisms (e.g., panels for 20060116 in Figures 5 and 6). The combination of these “nonhomologous” anomalous waves finally formed the signals shown in the wavelet spectra, and therefore the modulation of cyclones.

By looking closely at the sample cases mentioned above (cyclones in panels 20051221 and 20060116 in Figures 5 and 6), two distinct patterns of modulation were revealed. Although both had very strong signals over a 4- to 6-day period, their opposite signs suggested different dynamics. The cyclone of “20051221” (hereafter, Cyclone A) had a weakened long-period wavelet power and a strengthened short-time variation.

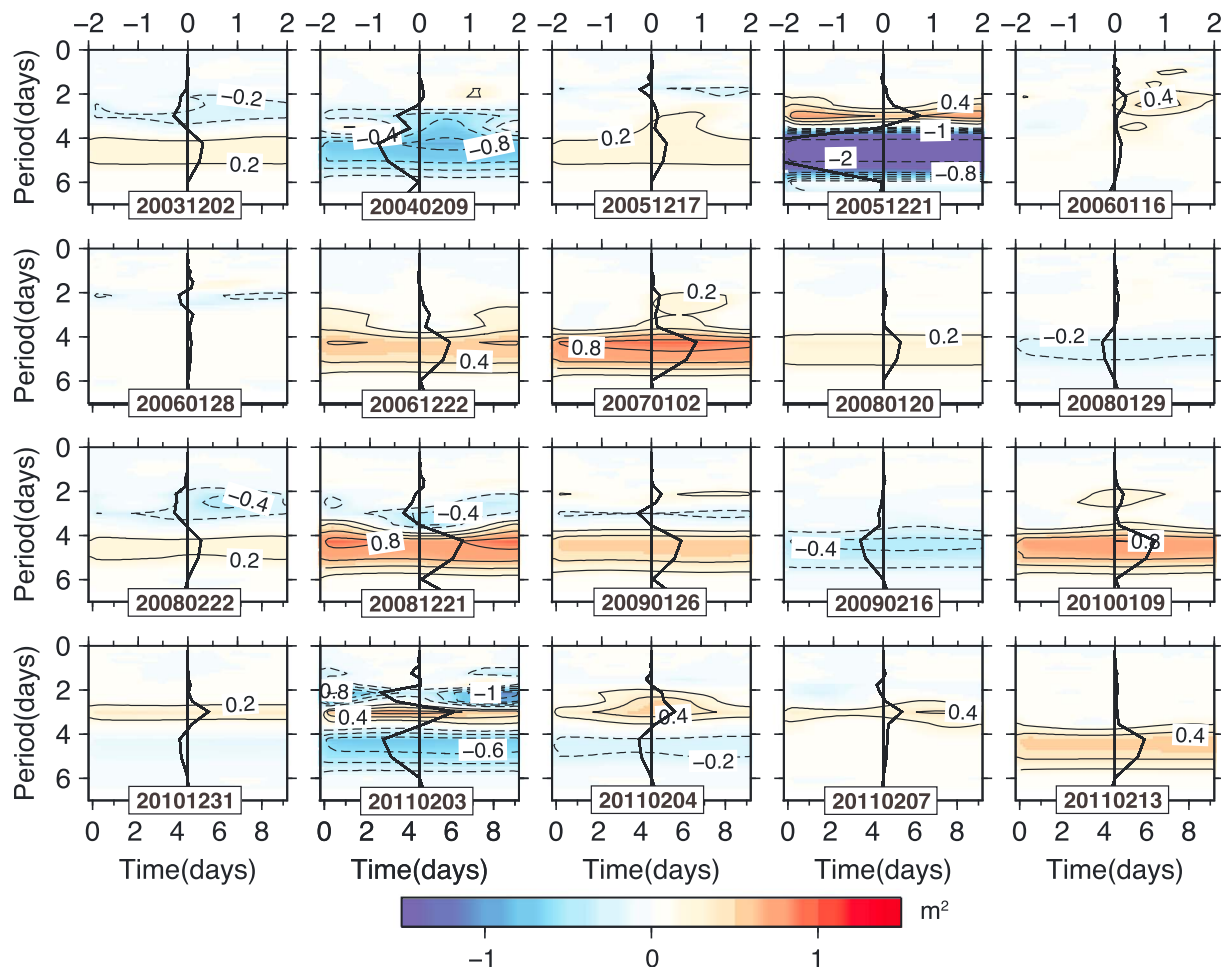


Figure 6. Same as Figure 5 but for values at the 500-hPa level.

It showed similar responses at different levels despite the signal being stronger (weaker) at the 500-hPa (850-hPa) level, suggesting that the modifications propagated from the higher levels. On the other hand, the cyclone of “20060116” (hereafter, Cyclone B) showed the same positive signals among different periods at a lower level and a weaker positive signal over a short period at the 500-hPa level, suggesting that the modifications probably originated at lower levels. It was interesting to note that, with the same SST disturbance, different source-induced modifications were found. Therefore, we performed further analyses on these two sample cyclones to determine how the same SST anomaly could generate different modulations.

5. Detailed Modifications of Cyclones

5.1. Cyclone A

Figure 7a shows the detailed modifications of Cyclone A in its central SLP, CDR, and path. In the CNTL runs, it had a minimum central SLP of 954.3 hPa and a maximum CDR of over 2.00 Bergeron. It formed (or was first detected by our algorithm) over the Sea of Japan on 25 December. Thereafter, it developed very quickly and moved eastward to the Pacific Ocean until it reached the eastern boundary of our domain. In the LSST runs, the central SLP anomaly (LSST-CNTL runs) of Cyclone A oscillated during its life span (dashed curve in the right panel of Figure 7a). The change in SLP was small but still large enough to modify the deepening rate clearly, which met our criteria. A similar oscillation was observed in the CDR time series (shown by the dark and light gray shading in the lower right graph). However, it seems likely that the cyclone path in the LSST runs was almost identical to that in the CNTL runs.

A similar pattern was observed in the SD of the 850-hPa geopotential height (Figure 8a). The increasing SD, which indicated the developing cyclone in the left panel, basically followed the cyclone paths detected by the

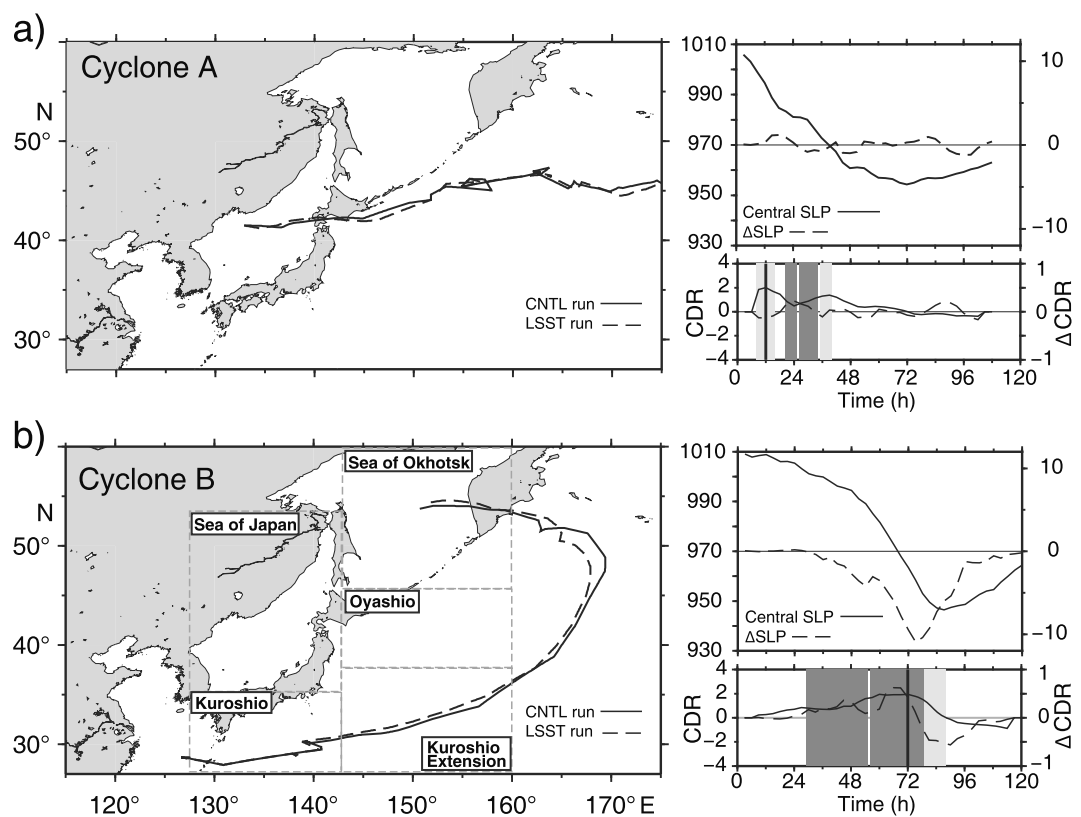


Figure 7. General details of Cyclones A and B in the CNTL and LSST runs, respectively. The right panels show the temporal evolution of the central SLP and CDR in the CNTL runs (solid curves; see the right ordinate of both panels) and their differences between two runs (LSST-CNTL runs, dashed curves; see the right ordinate in each panel). The strengthening (weakening) period is represented by the dark (light) gray shading in the CDR panel (see the text in section 4). The five regions selected for Figure 15 are indicated by the boxes surrounded by gray dashed lines. CDR = cyclone deepening rate; SLP = sea-level pressure.

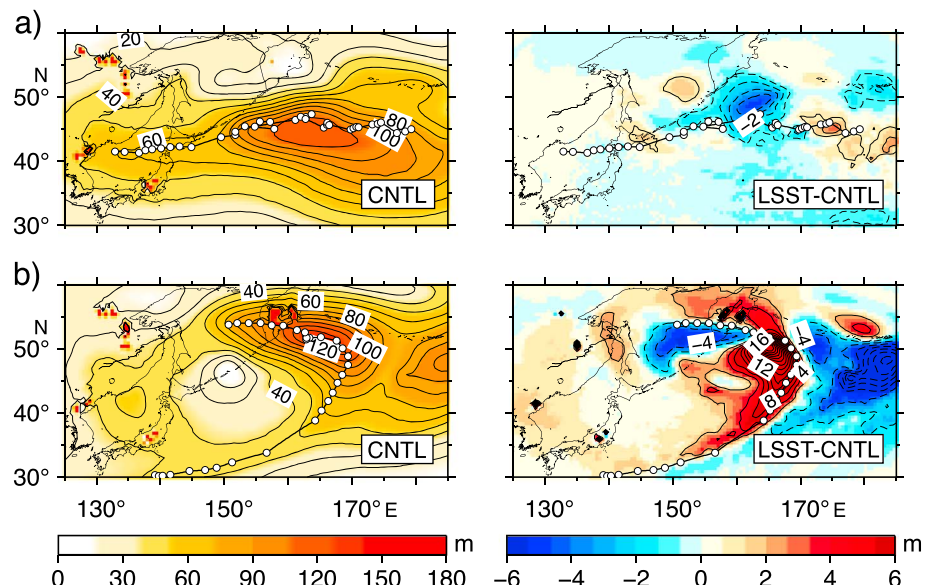


Figure 8. The activity of Cyclones A (a) and B (b). The left panels represent the standard deviation of geopotential height at the 850-hPa level in the CNTL runs, while the right panels show their differences between the sensitivity experiments (LSST-CNTL runs). Contour intervals are 10 m in the left panels, and 1 m in the right panels, except for the lower right panel where the interval is 2 m. Cyclone paths determined by the minimal SLP in the CNTL runs are shown by the black curves and white dots every 3 hr.

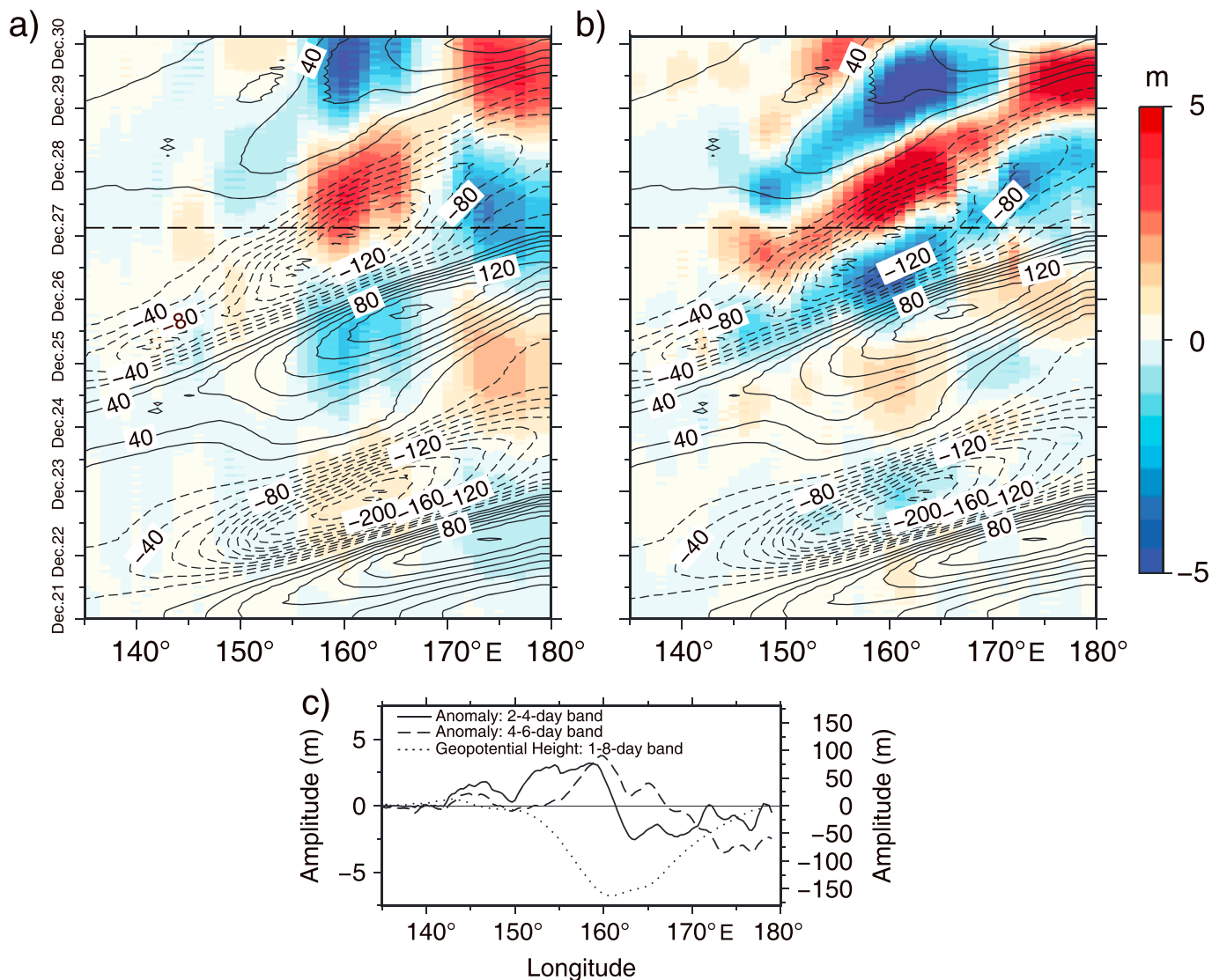


Figure 9. Hovmöller diagrams of the band-pass filtered geopotential height in Cyclone A's case. The contours indicate the baroclinic waves (i.e., cyclone) shown by the 1- to 8-day band-pass filtered geopotential height at the 850-hPa level in the CNTL run. Note that the same contour maps are depicted in both panels. The colored shading denotes the anomalies (LSST-CNTL runs) on time scales of (a) the 4- to 6-day band and (b) the 2- to 4-day band. Contour intervals are 20 m in both panels. Panel (c) denotes the waveforms of the short duration anomaly (solid curve), long duration anomaly (dashed curve), and the 1- to 8-day band-pass filtered geopotential height in the CNTL runs (dotted curve) along the dashed line in the upper panels.

SLP-based tracking algorithm, while the SD anomalies were consistent with the changes in CDRs (right panels of Figure 7a). The alternative appearance of the positive and negative SD anomalies along the path (upper right panel) suggests the possible superposition of multiple waves, which also showed good agreement with the wavelet spectra.

The "wave-like" anomalies revealed in Cyclone A could be clearly seen by the band-pass filtered geopotential heights (second-order Butterworth filter) around the frequencies revealed in the wavelet spectra. Compared with the scale of the passing cyclone (contours in Figures 9a and 9b), the long duration anomaly (colored shading in Figure 9a) had the same wavelength as the cyclone itself (Figure 9c). The phase of the geopotential height was almost the opposite before 25 December but was then shifted by $\sim \pi/2$. This result was consistent with the negative SD anomalies in the right panel of Figure 8a and the reduced wavelet spectra of the 4.5-day period activities. After the phase shift, the same propagation speed of those the anomalies revealed in the latter half of the Cyclone A period suggested that the path of the cyclone in the LSST run was slightly modified from that in the CNTL runs. Conversely, the short-duration anomalous wave

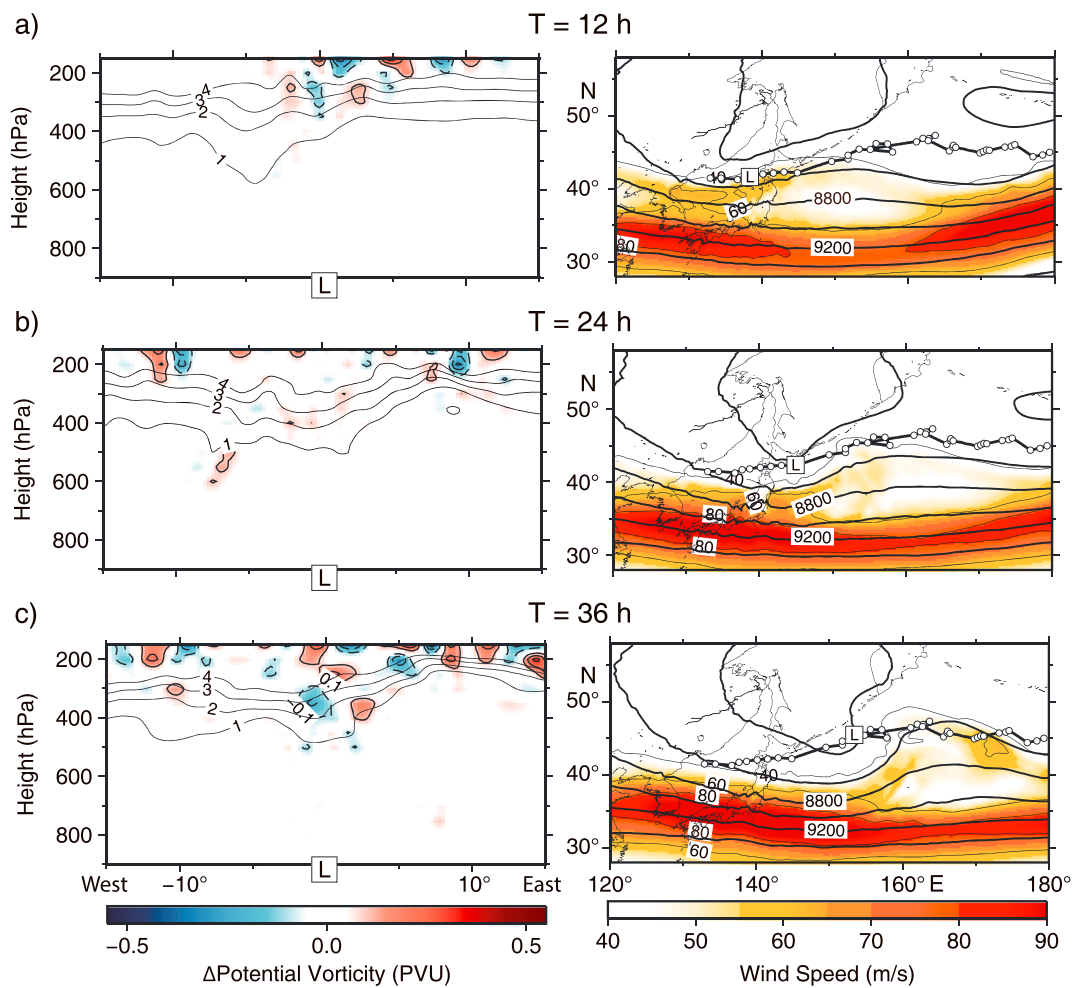


Figure 10. Zonal cross section of the potential vorticity (PV) around Cyclone A's center (left panels, meridionally averaged within $\pm 5^\circ$ latitude) and the wind speed and geopotential height at the 300-hPa level along with the cyclone's path (right panels). Cyclone centers at different time stages are shown by "L." (a) $T = 12$ hr, (b) $T = 24$ hr, and (c) $T = 36$ hr, where $T = 0$ represents the time when the cyclone was first identified. The left panels show the PV in the CNTL runs (thin contour) and its anomalies (LSST-CNTL runs, colored shading and thick contour). Right panels show the geopotential height (thick contour) and wind speed (colored shading and thin contour) at the 300-hPa level with the path of Cyclone A. Contour intervals are 1 PVU, 0.1 PVU, 200 m, and 20 m/s, respectively, where $1 \text{ PVU} = 10^{-6} \text{ m}^2 \cdot \text{K} \cdot \text{s}^{-1} \cdot \text{kg}^{-1}$.

(colored shading in Figure 9b) had a wavelength of approximately half of the baroclinic wave (Figure 9c), which corresponded to the increased 3-day signals in the wavelet power spectra (panels 20051221 in Figures 5 and 6). Despite the two anomalous waves described above, several mesoscale waves could also be seen in both the long-duration and the short-duration anomalies (see the short wavy oscillations in Figure 9c). All of these anomalous waves propagated eastward along with Cyclone A after its generation, which could therefore be regarded as the modulation of the cyclone due to the SST reduction over the Sea of Japan.

The results of the numerical experiment suggested that the source of the anomalous waves may be related to the modulations during the development of Cyclone A. Figure 10 shows the vertical structure of the potential vorticity (PV), and horizontal maps of the upper-level trough and jet during Cyclone A's early stages. When Cyclone A was generated over the Sea of Japan, its lower center was located beneath the edge of a weak jet streak, east of the large PV field (right panel in Figure 10a). Then it traveled eastward away from the jet streak (Figure 10b) and was overlapped by the PV maximum (Figures 10b and 10c) accompanied by a fast deepening (Figure 7a). During this transport, the positive and negative PV anomalies were simultaneously generated in the upper levels. These anomalies were absent before the cyclone's generation (not shown). Thereafter, these anomalies were enhanced and were advected along with the cyclone's propagation (left panels of Figure 10).

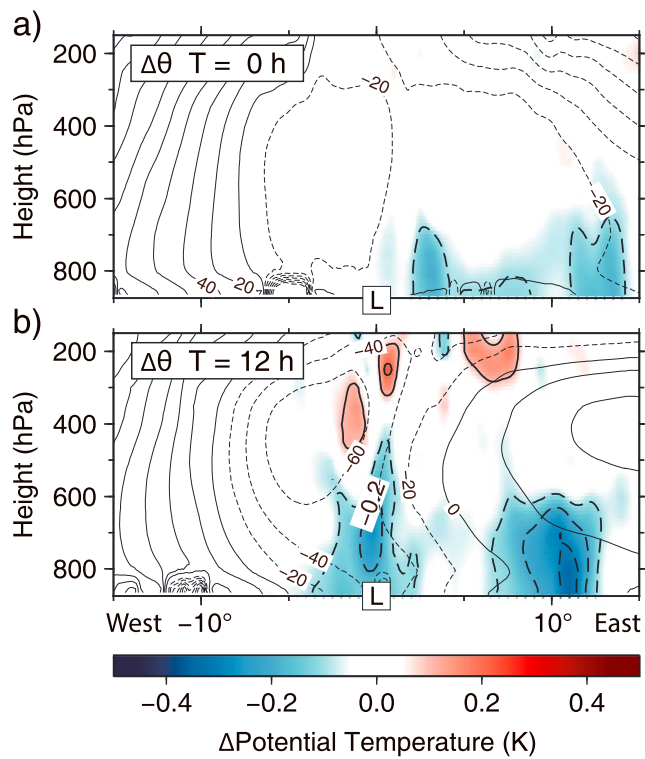


Figure 11. Zonal cross section of the potential temperature (θ) anomalies (LSST-CNTL, colored shading and thick contours) during Cyclone A's early stages, (a) $T = 0$ h and (b) $T = 12$ hr. The thin contours indicate the geopotential height deviations from the longitudinal average in the CNTL runs. Values were meridionally averaged within $\pm 5^\circ$ latitude. Contour intervals are 0.1 K and 20 m.

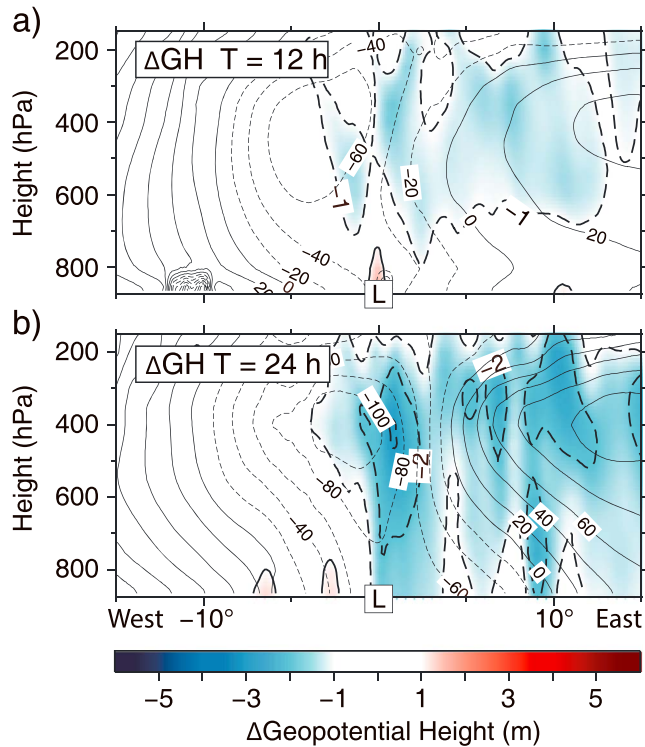


Figure 12. Same as Figure 11 but for the anomalies of geopotential heights 12 hr later, (a) $T = 12$ hr and (b) $T = 24$ hr. Contour intervals are 1 and 20 m.

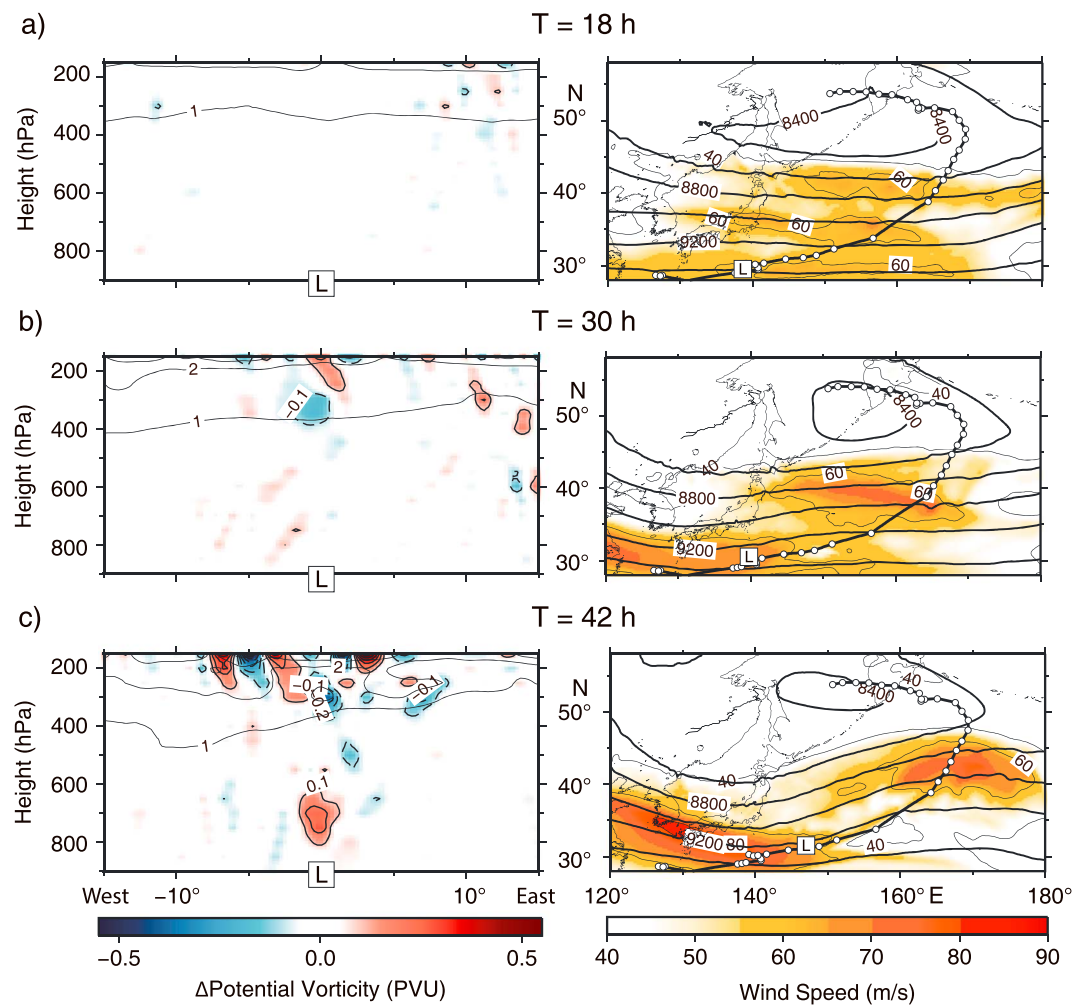


Figure 13. Same as Figure 10 but for Cyclone B. (a) $T = 18\text{ hr}$, (b) $T = 30\text{ hr}$, and (c) $T = 42\text{ hr}$.

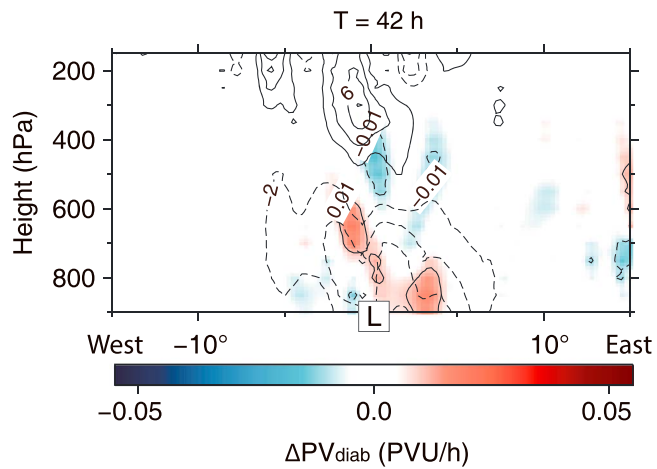


Figure 14. Cross section of the PV tendency (colored shading) induced by the anomalous diabatic heating (LSST-CNTL) and the difference in the geopotential height between LSST and CNTL runs (LSST-CNTL runs, contour) at $T = 42\text{ hr}$ of Cyclone B. Values were meridionally averaged within $\pm 5^\circ$ latitude. Contour intervals are 2 m and 0.01 PVU/hr.

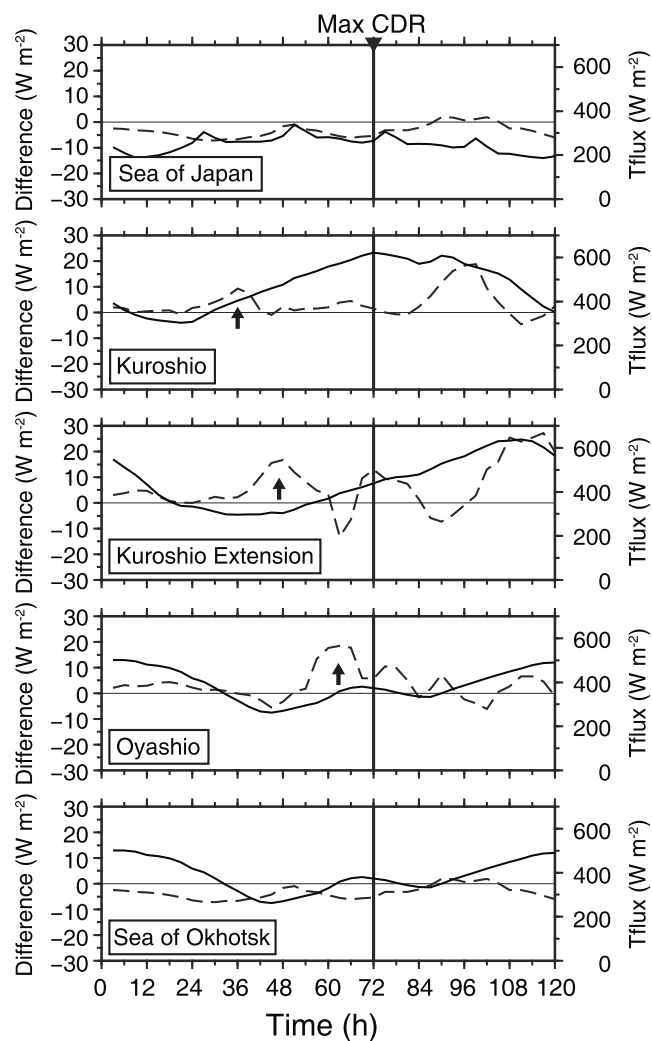


Figure 15. Time series of the turbulent heat fluxes averaged over the five regions (Figure 10) during Cyclone B's lifetime. The solid curves show the values in the CNTL run, and the dashed curves are the differences (LSST-CNTL runs). The arrows indicate the time when the cyclone-related positive anomalies appeared. The letters “Max CDR” indicate the time of the maximum CDR. CDR = cyclone deepening rate.

The characteristics of Cyclone A suggested that it was mainly developed by the upper-level PV advection, which is the main forcing mechanism in OJ-type cyclones (e.g., Kuwano-Yoshida & Asuma, 2004, 2008). Therefore, anomalies in the upper-level PV field could modulate the cyclone during cyclogenesis, although the source of these anomalies remains unclear.

In addition to the influence of upper-level PV anomalies, temperature advection may also play a role in the cyclone modulation. As shown in Figure 11, the negative SST anomaly led to a reduced air temperature over the Sea of Japan (Figure 11a), which was consistent with the results in section 3.2. The potential temperature anomaly remained in the lower levels before Cyclone A was generated, but it soon spread to higher levels accompanied by the upward motion in the ascent phase of the baroclinic wave (Figure 11b). It is likely that the temperature anomalies also contributed to the generation of anomalies in geopotential height by stabilizing the atmosphere, hence the weakening of the baroclinic wave (Figure 12). The dynamics revealed here is similar to the results reported by Yamamoto (2013), except for the unchanged diabatic heating rate because no obvious lower-level PV anomaly was found in Cyclone A's case. This was probably due to the aforementioned upper-PV forced rapid deepening of Cyclone A and the small SST anomaly that we applied.

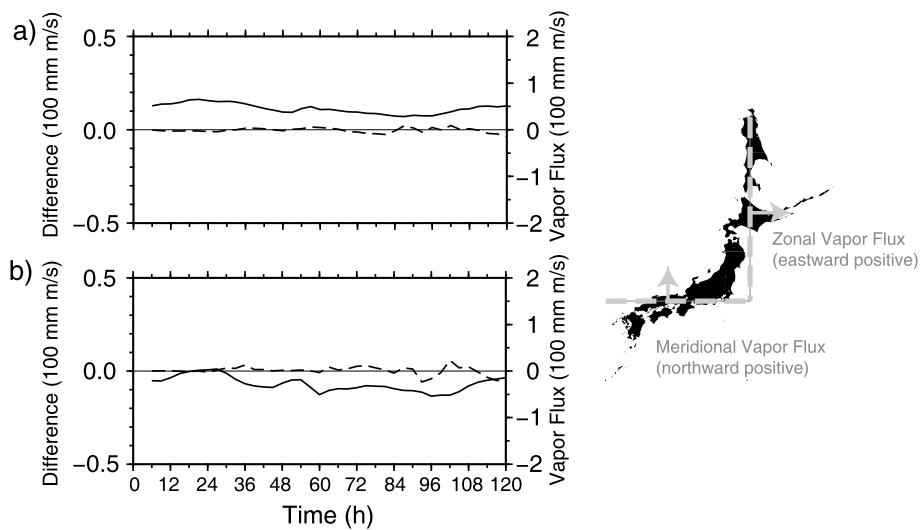


Figure 16. Time series of the vertically integrated (1,000- to 300-hPa) vapor fluxes across the eastern (a; 142.5°E, 35°–54°N) and southern (b; 127°–142.5°E, 35°N) boundaries of the Sea of Japan; see the map on the right side for the locations of the boundaries. Positive values show the eastward fluxes in panel (a) and the northward fluxes in panel (b); see also the direction of the arrows. Solid curves show the values in the CNTL run and the dashed curves are the differences (LSST-CNTL runs); see the left ordinates.

5.2. Cyclone B

Cyclone B formed over the East China Sea (identified on 20 January 2006; Figure 7b) and passed south of Japan with a minimum central SLP of 946.4 hPa and a maximum CDR of 1.96 Bergeron. It developed slowly in the first 2 days near the Sea of Japan and then developed over the Pacific Ocean. It traveled northeastward over most of its lifetime but then abruptly turned westwards to the Sea of Okhotsk during the final section of its path. Unlike Cyclone A, Cyclone B was greatly intensified (decreased by >10 hPa) in the LSST runs and its path was also shifted poleward (compare the solid and dashed curves in Figure 7b). Positive and negative anomalies in the SD of geopotential height, exhibited on each side of its path (Figure 8b), were consistent with the changing path observed from center tracking (broken curve in Figure 7b).

Cyclone B developed under the jet streak in its early stages, where the upper-level PV was relatively small (Figure 13) compared with that of Cyclone A. Positive and negative PV anomalies were also generated at higher levels when Cyclone B passed near the Sea of Japan, as observed in Cyclone A. However, a positive PV anomaly was generated at lower levels (Figure 13c), which was absent in the case of Cyclone A. According to previous studies (e.g., Fu et al., 2014; Hirata et al., 2015), it is reasonable to consider that this lower-level PV anomaly was strongly related to diabatic processes. To evaluate this, we calculated the diabatic heating rate, Q_d , near the cyclone center based on the following formula:

$$Q_d = \frac{\partial \theta}{\partial t} + \mathbf{U} \cdot \nabla \theta, \quad (2)$$

where θ and \mathbf{U} are the potential temperature and the three-dimensional wind vectors, respectively, and the other notations are standard. Then, following Tamarin and Kaspi (2016), the PV tendency induced by the diabatic heating can be approximately estimated by the following:

$$\frac{dPV_{\text{diab}}}{dt} = -g(f + \zeta) \frac{\partial}{\partial p} Q_d, \quad (3)$$

where g is the gravitational acceleration, f is the planetary vorticity, and ζ is the relative vorticity.

As shown in Figure 14, the diabatic heating induced PV production rates were in good agreement with the PV anomalies found in the LSST runs (Figure 13c). The associated positive (negative) geopotential height anomalies in upper (lower) levels also agreed well with the signals revealed in the wavelet spectra, suggesting that Cyclone B was intensified due to the enhanced diabatic heating. Note that the poleward shifting of Cyclone B could be explained by the Q_d -PV-related processes as described by Tamarin and Kaspi (2016).

To determine how a cooled Sea of Japan could enhance diabatic heating, the temporal evolution of the surface turbulent heat fluxes averaged in five regions (boxes surrounded by gray lines in Figure 7b) is shown in Figure 15. Although only negative anomalies were found over the Sea of Japan due to the negative SST anomaly, the other four regions had positive values. First, a positive heat flux anomaly appeared in the Kuroshio region (see the arrows in the Kuroshio panel in Figure 15) when Cyclone B was first recognized in the domain. The cyclone had not yet been modified sufficiently at this moment (Figure 7b) in comparison with the anomalous magnitude found subsequently in other areas. Strong positive anomalies then appeared in the Kuroshio Extension and the Oyashio region due to the intensified cyclone propagating eastward following the path shown in Figure 7b. The enhanced turbulent heat fluxes were probably caused by colder air spreading from the SST-reduced Sea of Japan, as shown in Figure 3a, and this nonlocal effect finally intensified Cyclone B. Further evidence can be found in the unchanged moisture supply that crossed the eastern and southern boundaries of the Sea of Japan (Figure 16), which suggested that the extra moisture did not originate from the Sea of Japan.

According to the above results, the process can be summarized as follows. The negative SST anomaly initially reduced the local surface heating in the Sea of Japan, especially in the period of the affected cyclones when intensive northwesterly winds strengthened the link between the Sea of Japan and the atmosphere above it. Then the Sea of Japan acted as a “source” of the cold anomaly (but not the source of the reduced moisture), allowing the cold air to spread onto the surrounding areas that induced the enhancement of upward heat fluxes from the ocean. Cyclone B was therefore intensified due to the enhanced upward heat fluxes over the south of Japan (Figures 15 and S2a). Thereafter, the area with enhanced heat fluxes moved eastward due to cyclone propagation but remained in the northwestern sector (cold sector) of Cyclone B (Figure S2b). However, the enhanced heat fluxes along the cyclone path were unlikely to be caused only by the cold air mass carried directly from the Sea of Japan but were also likely influenced by the positive feedback from the interaction between cyclones and oceans. As a result, the influence of the cooled Sea of Japan was transported to a much wider area by the modulated propagating cyclone itself. Therefore, besides the local effect on the passing cyclone, the Sea of Japan also played a remote role in distant regions via the modified cyclones, as suggested by Yamamoto (2013).

6. Conclusions

In this study, we investigated the effects of the cyclone-induced SST anomaly in the Sea of Japan on subsequent cyclones based on a regional numerical model. We designed a set of sensitivity experiments for 26 cyclones with the winter climatological mean SST (CNTL runs; contour in Figure 1) and an extra negative SST anomaly (LSST runs; colored shading in Figure 1).

Twenty of the 26 cyclones responded well to the SST anomaly, while the remaining six cyclones were nearly unaffected (Figure 2). In conclusion, the low-level trough (therefore, the northwesterly winds) was found to be the controlling factor of cyclone sensitivity and therefore, the connection between two consecutive cyclones. The deeper (shallower) the trough, the stronger (weaker) the northwesterlies, which enhanced cold air intrusion over the Sea of Japan. This strong cold-air intrusion generated a band of strong baroclinity over the Kuroshio, south of Japan (Figure 4a), and potentially resulted in the formation of storms, making cyclones more sensitive to the underlying SST. In addition, with (without) the dominance of the cold air mass, a thicker (thinner) convective layer encouraged (restrained) the upward penetration of the marine atmospheric boundary layer over the Sea of Japan (Figure 4b) and therefore improved the connections between cyclones and the lower boundary conditions.

The differences in CDRs and wavelet spectra demonstrated the existence of both strengthened and weakened cyclones. The similar signals of the wavelet spectra suggested that the dynamical processes induced by SST anomalies could be found among the 20 affected cyclones as well as the two cyclones analyzed in detail.

Our results showed that the wave-like pattern of Cyclone A was generated by the linear superposition of anomalous waves with different periods and scales. The anomalies in geopotential heights, generated by the upper-level PV anomalies and the temperature advection, were weak in the early stages but were then rapidly enhanced as they were advected by the deepening cyclone, coupled with the large upper-level PV. In addition to the modifications at the synoptic scale, some mesoscale waves were also generated and traveled together with the cyclone.

The path-shifting pattern revealed in Cyclone B was strongly related to cyclone intensification. A positive lower-level PV anomaly generated by the intense diabatic heating was found near the cyclone center. Although the SST anomaly reduced the surface heating locally over the Sea of Japan, it allowed a colder air mass to spread over the surrounding areas. This colder air mass enhanced the surface heating and moisture supplement over the Kuroshio region and therefore intensified the cyclone passing aloft.

We conclude that a cyclone can modulate subsequent cyclones via cooling of the Sea of Japan, even through a small SST disturbance. The processes may act in different ways and generate upper- and/or lower-level anomalies, depending on the atmospheric background and cyclone structures. The deepening of cyclones also helps the development of anomalous waves. Comparing the different processes found in two sample cases, the dynamics of the cyclone itself may play an important role in the pattern of cyclone responses (e.g., Kuwano-Yoshida & Asuma, 2004), although this requires further study. Our results revealed the possible modification of cyclones passing near the cooled Sea of Japan; however, it remains unclear how a small SST disturbance could generate upper-level PV anomalies, which will be the next stage of this research.

Appendix A: Ensemble Simulations for the Validation of Results

In this study, the SST anomaly applied to the Sea of Japan was, on average, very small (-0.25°C) compared with the meridional SST difference ($\sim 16\text{ K}$; see Figure 1), and our results might therefore be vulnerable to small SST fluctuations, which could potentially develop into other anomalies over time. Thus, we need to examine whether our results are robust compared with SST fluctuations, especially when the SST anomaly used in the LSST runs was much smaller than that in other similar studies (e.g., Booth et al., 2012; Yamamoto, 2013; Yamamoto & Hirose, 2007).

To validate our modeling results, we conducted a set of 10-member ensemble simulations for LSST runs, forced by different SST anomalies. The “new” SST anomalies used in each member were a set of combinations of “old” anomalies (colored shading in Figure 1) and normally distributed random noise with the same standard deviation as the old anomaly ($\sim 0.1^{\circ}\text{C}$).

Despite the small fluctuations due to the slightly different lower boundary conditions, in all experiments a similar poleward shift and intensified cyclone were observed (Figure S3). In Figure S4, the ensemble means (right panel) of the anomalies of the diabatic heating rate, the PV tendency due to the diabatic heating, and vertical velocity (only results over the 95% confidence level were plotted) were all similar to those in the single run (left panel). Note that, as mentioned in section 5.2, the poleward shifting of Cyclone B was caused by the positive anomalies of the diabatic heating and PV tendency, and an upward velocity was observed on the northern side of the cyclone center (“L” in figures).

Therefore, our conclusions were considered to be robust. Moreover, these results also suggested that, at least in a small marginal sea, the negative SST anomaly itself is important for synoptic scale cyclones, as well as the horizontal SST distribution, such as the oceanic frontal structure (e.g., Yamamoto & Hirose, 2007).

Acknowledgments

We are grateful to H. Hirata for his help on data analysis. Authors also thank two anonymous reviewers for their fruitful comments and suggestions, which greatly improved the quality of this paper. The meteorological data for the model initial condition are available on the ftp database of NCEP FNL (<https://rda.ucar.edu/datasets/ds083.2/>), and the lower boundary conditions, including the climatological winter SST and SST anomaly, are available on Zenodo.org (<https://doi.org/10.5281/zenodo.1136042>).

References

- Banzon, V., Smith, T. M., Chin, T. M., Liu, C., & Hankins, W. (2016). A long-term record of blended satellite and in situ sea-surface temperature for climate monitoring, modeling and environmental studies. *Earth System Science Data*, 8(2), 165–176. <https://doi.org/10.5194/essd-8-165-2016>
- Booth, J. F., Thompson, L., Patoux, J., & Kelly, K. A. (2012). Sensitivity of midlatitude storm intensification to perturbations in the sea surface temperature near the Gulf Stream. *Monthly Weather Review*, 140, 1241–1256. <https://doi.org/10.1175/MWR-D-11-00195.1>
- Brayshaw, D. J., Hoskins, B., & Blackburn, M. (2008). The storm-track response to idealized sst perturbations in an aquaplanet GCM. *Journal of the Atmospheric Sciences*, 65(9), 2842–2860. <https://doi.org/10.1175/2008JAS2657.1>
- Catto, J., Jakob, C., Berry, G., & Nicholls, N. (2012). Relating global precipitation to atmospheric fronts. *Geophysical Research Letters*, 39, L10805. <https://doi.org/10.1029/2012GL051736>
- Chang, E. K., Lee, S., & Swanson, K. L. (2002). Storm track dynamics. *Journal of Climate*, 15(16), 2163–2183.
- Chelton, D. B., & Xie, S.-P. (2010). Coupled ocean-atmosphere interaction at oceanic mesoscales. *Oceanography*, 23, 52–69. <https://doi.org/10.5670/oceanog.2010.05>
- Chen, S. S., Zhao, W., Tenerelli, J. E., Evans, R. H., & Halliwell, V. (2001). Impact of the AVHRR sea surface temperature on atmospheric forcing in the Japan/East sea. *Geophysical research letters*, 28(24), 4539–4542.
- Flaounas, E., Kotroni, V., Lagouvardos, K., & Flaounas, I. (2014). Cyclotrack (v1. 0)—tracking winter extratropical cyclones based on relative vorticity: Sensitivity to data filtering and other relevant parameters. *Geoscientific Model Development*, 7(4), 1841–1853. <https://doi.org/10.5194/gmd-7-1841-2014>
- Fu, S., Sun, J., & Sun, J. (2014). Accelerating two-stage explosive development of an extratropical cyclone over the Northwestern Pacific Ocean: A piecewise potential vorticity diagnosis. *Tellus A*, 66, 23210. <https://doi.org/10.3402/tellusa.v66.23210>
- Hirata, H., Kawamura, R., Kato, M., & Shinoda, T. (2015). Influential role of moisture supply from the Kuroshio/Kuroshio Extension in the rapid development of an extratropical cyclone. *Monthly Weather Review*, 143(10), 4126–4144. <https://doi.org/10.1175/MWR-D-15-0016.1>

- Hirose, N., Nishimura, K., & Yamamoto, M. (2009). Observational evidence of a warm ocean current preceding a winter teleconnection pattern in the Northwestern Pacific. *Geophysical Research Letters*, 36, L09705. <https://doi.org/10.1029/2009GL037448>
- Hodges, K. (1999). Adaptive constraints for feature tracking. *Monthly Weather Review*, 127(6), 1362–1373. [https://doi.org/10.1175/1520-0493\(1999\)127<1362:ACFT>2.0.CO;2](https://doi.org/10.1175/1520-0493(1999)127<1362:ACFT>2.0.CO;2)
- Inatsu, M. (2009). The neighbor enclosed area tracking algorithm for extratropical wintertime cyclones. *Atmospheric Science Letters*, 10(4), 267–272. <https://doi.org/10.1002/asl.238>
- Isobe, A., & Kako, S. (2012). A role of the yellow and east China seas in the development of extratropical cyclones in winter. *Journal of Climate*, 25(23), 8328–8340. <https://doi.org/10.1175/JCLI-D-11-00391.1>
- Kelly, K. A., Small, R. J., Samelson, R., Qiu, B., Joyce, T. M., Kwon, Y.-O., & Cronin, M. F. (2010). Western boundary currents and frontal air–sea interaction: Gulf stream and Kuroshio Extension. *Journal of Climate*, 23(21), 5644–5667. <https://doi.org/10.1175/2010JCLI3346.1>
- König, W., Sausen, R., & Sielmann, F. (1993). Objective identification of cyclones in GCM simulations. *Journal of Climate*, 6(12), 2217–2231.
- Kuwano-Yoshida, A., & Asuma, Y. (2004). Structures and environment of explosively developing extratropical cyclones in the Northwestern Pacific region. *Monthly Weather Review*, 132(5), 1121–1142. [https://doi.org/10.1175/1520-0493\(2004\)132<1121:SAEOD>2.0.CO;2](https://doi.org/10.1175/1520-0493(2004)132<1121:SAEOD>2.0.CO;2)
- Kuwano-Yoshida, A., & Asuma, Y. (2008). Numerical study of explosively developing extratropical cyclones in the Northwestern Pacific region. *Monthly Weather Review*, 136, 712–740. <https://doi.org/10.1175/2007MWR2111.1>
- Kwon, Y.-O., Alexander, M. A., Bond, N. A., Frankignoul, C., Nakamura, H., Qiu, B., & Thompson, L. A. (2010). Role of the Gulf Stream and Kuroshio-Oyashio systems in large-scale atmosphere-ocean interaction: A review. *Journal of Climate*, 23(12), 3249–3281. <https://doi.org/10.1175/2010JCLI3343.1>
- Ma, X., Chang, P., Saravanan, R., Montuoro, R., Nakamura, H., Wu, D., et al. (2017). Importance of resolving Kuroshio front and eddy influence in simulating the North Pacific storm track. *Journal of Climate*, 30(5), 1861–1880. <https://doi.org/10.1175/JCLI-D-16-0154.1>
- Masunaga, R., Nakamura, H., Miyasaka, T., Nishii, K., & Qiu, B. (2016). Interannual modulations of oceanic imprints on the wintertime atmospheric boundary layer under the changing dynamical regimes of the Kuroshio Extension. *Journal of Climate*, 29(9), 3273–3296. <https://doi.org/10.1175/JCLI-D-15-0545.1>
- NCEP (2000). Operational model global tropospheric analyses continuing from July 1999, Research Data Archive at the National Center for Atmospheric Research, Computational and Information Systems Laboratory, Boulder, CO. Retrieved from <http://rda.ucar.edu/datasets/ds083>. <https://doi.org/10.5065/D6M043C6>
- Nakamura, H. (1992). Midwinter suppression of baroclinic wave activity in the pacific. *Journal of the Atmospheric Sciences*, 49(17), 1629–1642.
- Nakamura, H., Izumi, T., & Sampe, T. (2002). Interannual and decadal modulations recently observed in the Pacific storm track activity and East Asian Winter Monsoon. *Journal of Climate*, 15(14), 1855–1874. [https://doi.org/10.1175/1520-0442\(2002\)015<1855:IADMRO>2.0.CO;2](https://doi.org/10.1175/1520-0442(2002)015<1855:IADMRO>2.0.CO;2)
- Nakamura, H., Sampe, T., Tanimoto, Y., & Shimpo, A. (2004). Observed associations among storm tracks, jet streams and midlatitude oceanic fronts, Earth's climate: The ocean–atmosphere interaction. *Geophysical Monograph*, 147, 329–345. <https://doi.org/10.1029/147GM18>
- Parfitt, R., Czaja, A., Minobe, S., & Kuwano-Yoshida, A. (2016). The atmospheric frontal response to SST perturbations in the Gulf Stream region. *Geophysical Research Letters*, 43, 2299–2306. <https://doi.org/10.1002/2016GL067723>
- Pinto, J. G., Ulbrich, U., Leckebusch, G., Spangehl, T., Reyers, M., & Zacharias, S. (2007). Changes in storm track and cyclone activity in three SRES ensemble experiments with the ECHAM5/MPI-OM1 GCM. *Climate Dynamics*, 29(2-3), 195–210. <https://doi.org/10.1007/s00382-007-0230-4>
- Putrasahan, D. A., Miller, A. J., & Seo, H. (2013). Isolating mesoscale coupled ocean–atmosphere interactions in the Kuroshio Extension region. *Dynamics of Atmospheres and Oceans*, 63, 60–78. <https://doi.org/10.1016/j.dynatmoce.2013.04.001>
- Reynolds, R. W., Smith, T. M., Liu, C., Chelton, D. B., Casey, K. S., & Schlax, M. G. (2007). Daily high-resolution-blended analyses for sea surface temperature. *Journal of Climate*, 20(22), 5473–5496. <https://doi.org/10.1175/2007JCLI1824.1>
- Roeber, P. J. (1984). Statistical analysis and updated climatology of explosive cyclones. *Monthly Weather Review*, 112(8), 1577–1589. [https://doi.org/10.1175/1520-0493\(1984\)112<1577:SAAUCO>2.0.CO;2](https://doi.org/10.1175/1520-0493(1984)112<1577:SAAUCO>2.0.CO;2)
- Sampe, T., Nakamura, H., Goto, A., & Ohfuchi, W. (2010). Significance of a midlatitude SST frontal zone in the formation of a storm track and an eddy-driven westerly jet. *Journal of Climate*, 23(7), 1793–1814. <https://doi.org/10.1175/2009JCLI3163.1>
- Seo, H., Kwon, Y.-O., & Park, J.-J. (2014). On the effect of the east/japan sea stt variability on the North Pacific atmospheric circulation in a regional climate model. *Journal of Geophysical Research: Atmospheres*, 119, 418–444. <https://doi.org/10.1002/2013JD020523>
- Shaw, T., Baldwin, M., Barnes, E., Caballero, R., Garfinkel, C., Hwang, Y.-T., et al. (2016). Storm track processes and the opposing influences of climate change. *Nature Geoscience*, 9, 656–664. <https://doi.org/10.1038/ngeo2783>
- Skamarock, W. C., Klemp, J. B., Dudhia, J., Gill, D. O., Barker, D. M., Wang, W., & Powers, J. G. (2008). A description of the advanced research WRF version 2 (*Tech. rep.*) Boulder, Colorado, USA: National Center for Atmospheric Research. NCAR Technical Note NCAR/TN-475+STR <https://doi.org/10.5065/D68S4MVH>
- Small, R., Xie, S., O'Neill, L., Seo, H., Song, Q., Cornillon, P., et al. (2008). Air-sea interaction over ocean fronts and eddies. *Dynamics of Atmospheres and Oceans*, 45(3), 274–319. <https://doi.org/10.1016/j.dynatmoce.2008.01.001>
- Tamarin, T., & Kaspi, Y. (2016). The poleward motion of extratropical cyclones from a potential vorticity tendency analysis. *Journal of the Atmospheric Sciences*, 73(4), 1687–1707. <https://doi.org/10.1175/JAS-D-15-0168.1>
- Torrence, C., & Compo, G. P. (1998). A practical guide to wavelet analysis. *Bulletin of the American Meteorological Society*, 79(1), 61–78. [https://doi.org/10.1175/1520-0477\(1998\)079<0061:APGTWA>2.0.CO;2](https://doi.org/10.1175/1520-0477(1998)079<0061:APGTWA>2.0.CO;2)
- Willison, J., Robinson, W. A., & Lackmann, G. M. (2013). The importance of resolving mesoscale latent heating in the North Atlantic storm track. *Journal of the Atmospheric Sciences*, 70(7), 2234–2250. <https://doi.org/10.1175/JAS-D-12-0226.1>
- Yamamoto, M. (2013). Effects of a semi-enclosed ocean on extratropical cyclogenesis: The dynamical processes around the Japan Sea on 23–25 January 2008. *Journal of Geophysical Research: Atmospheres*, 118, 10,391–10,404. <https://doi.org/10.1002/jgrd.50802>
- Yamamoto, M., & Hirose, N. (2007). Impact of SST reanalyzed using OGCM on weather simulation: A case of a developing cyclone in the Japan Sea area. *Geophysical Research Letters*, 34, L05808. <https://doi.org/10.1029/2006GL028386>
- Yamamoto, M., & Hirose, N. (2011). Possible modification of atmospheric circulation over the Northwestern Pacific induced by a small semi-enclosed ocean. *Geophysical Research Letters*, 38, L03804. <https://doi.org/10.1029/2010GL046214>
- Yoshiike, S., & Kawamura, R. (2009). Influence of wintertime large-scale circulation on the explosively developing cyclones over the western North Pacific and their downstream effects. *Journal of Geophysical Research*, 114, D13110. <https://doi.org/10.1029/2009JD011820>
- Zhao, N., Iwasaki, S., Isobe, A., Lien, R.-C., & Wang, B. (2016). Intensification of the subpolar front in the Sea of Japan during winter cyclones. *Journal of Geophysical Research: Oceans*, 121, 2253–2267. <https://doi.org/10.1002/2015JC011565>